

## 3D NON-HYDROSTATIC MODELING OF BOTTOM AND BANK STABILITY SUBJECTED BY SHIP PROPELLER JETS

Vladimir Maderich<sup>1</sup>, Yulia Kanarska<sup>2</sup>, Scott Fenical<sup>3</sup>, Igor Brovchenko<sup>1</sup>, Kateryna Terletska<sup>1</sup> and Matteo Tirindelli<sup>3</sup>

A new three-dimensional numerical model is presented for prediction of propeller jet action from slowly maneuvering vessels. The non-hydrostatic free-surface model is based on the Reynolds averaged Navier-Stokes equations. The model is distinct from other known propeller jet models in that it describes fields of velocity, pressure, turbulence intensity and length scale in a given domain of arbitrary bottom and coastal topography. The results of simulations show good agreement with laboratory experiments in a tank with an inclined bottom (Schokking 2002) and field measurements with tug boats. It is concluded that the dynamic pressure gradient along the bottom can be a propeller wash factor that is comparable with bottom shear stress and can be responsible for stone displacement near the lowest part of the bottom slope where near-bottom velocities are not the largest.

### INTRODUCTION

In coastal engineering practice, strong flows generated by vessel propulsion systems (propellers and water jets) are known to cause significant impact to aquatic habitat, re-suspension of contaminated sediments and loading on nearshore structures. These strong currents affect the quality of sediments in marine industrial areas, and in some cases are the design conditions for bank and slope protection near marine terminals. These common engineering problems motivated the development and testing of the 3D, non-hydrostatic free-surface Vessel Hydrodynamics Propwash Unsteady (VH-PU) model. The model simulates these vessel-induced flows and bottom and bank stability subjected to ship propeller jets. Most of the known propeller wash models (Blaauw and Kaa, 1978; Fuehrer et al., 1987; Hamill, 1988; Verhey, 1983; Shepsis and Simpson, 2001) use the self-similar dependencies for a stationary jet in an unbounded domain, corrected for bottom effects. The present model describes unsteady, three-dimensional fields of velocities generated by ship propellers, turbulence intensity and length scale in the given domain of arbitrary bottom and coastal topography. The temporally and spatially varying bottom shear stresses that caused bottom erosion and damage to bottom habitat are calculated, as well as forces due to pressures on submerged boundaries. The model was developed on the basis of the non-hydrostatic model of Kanarska and Maderich (2003). The

---

<sup>1</sup> Ukrainian Center of Environmental and Water Projects, Glushkov Avenue, 42, Kiev, 03187, Ukraine

<sup>2</sup> Institute of Geophysics and Planetary Physics, University of California at Los Angeles, Hilgard Avenue, Los Angeles, CA, 90095, USA

<sup>3</sup> Coast & Harbor Engineering, Inc., 155 Montgomery St, Suite 608, San Francisco, CA 94104, USA

model version presented here allows calculation of hydrodynamic fields caused by propeller jets for stationary vessels with one or two propellers/jets.

**MODEL**

**Basic equations**

The 3-D Reynolds-averaged continuity and Navier-Stokes equations (RANS equations) describing the turbulent motion under large Reynolds numbers can be written as follows:

$$\frac{\partial u_i}{\partial x_i} = 0, \tag{1}$$

$$\frac{\partial u_i}{\partial t} + u_j \frac{\partial u_i}{\partial x_j} = -\frac{1}{\rho_0} \frac{\partial p}{\partial x_i} - \frac{\overline{\partial u'_i u'_j}}{\partial x_j} - g_i, \tag{2}$$

where  $x_i = (x,y,z)$  are Cartesian coordinates, axis  $z$  is directed upward,  $u_i = (u,v,w)$  are components of mean velocity. The primed symbols indicate the fluctuations,  $u'_i = (u',v',w')$ ;  $p$  is pressure;  $g_i = (0,0,g)$  is gravity;  $\rho_0$  is constant density. The Reynolds stresses are modeled using the eddy viscosity approach

$$\overline{u'_i u'_j} = -K_M \left( \frac{\partial u_i}{\partial x_j} + \frac{\partial u_j}{\partial x_i} \right) + \frac{1}{3} q^2 \delta_{ij}, \tag{3}$$

where eddy viscosity coefficient  $K_M = S_M q l$  is related with kinetic energy of turbulence  $q^2/2$  and length scale  $l$ . Here  $S_M$  is the model constant and  $\delta_{ij}$  is the Kronecker symbol.

The model of turbulence is the  $q - q^2 l$  model (Vollmers and Rotta 1977; Mellor and Yamada 1982):

$$\frac{\partial q^2}{\partial t} + u_j \frac{\partial q^2}{\partial x_j} = -2 \overline{u'_i u'_j} \frac{\partial u_i}{\partial x_j} + S_q \frac{\partial}{\partial x_j} q l \frac{\partial q^2}{\partial x_j} - 2 \frac{q^3}{B_1 l}, \tag{4}$$

$$\frac{\partial q^2 l}{\partial t} + u_j \frac{\partial q^2 l}{\partial x_j} = S_l \frac{\partial}{\partial x_j} q l \frac{\partial q^2 l}{\partial x_j} - E_1 \overline{u'_i u'_j} \frac{\partial u_i}{\partial x_j} - \frac{q^3}{B'_1} \left[ 1 + E_2 \left( \frac{l}{\kappa L} \right)^2 \right]. \tag{5}$$

The last term in square brackets in (5) is a wall function, which is necessary in  $q^2 - q^2 l$  model to correctly describe flow near the solid boundary. Here  $L$  is distance from the nearest solid boundary and  $\kappa$  is von Karman constant. The constants of the turbulence model  $B_1 = 17.14, B'_1 = 11.05, S_M = 0.387, E_1 = 1.96, E_2 = 1.33, S_q = S_l = 0.566$  were adopted from (Vollmers and Rotta 1977).

### Boundary conditions

The kinematic boundary condition on the free surface  $z = \eta(x, y, t)$  is

$$\frac{\partial \eta}{\partial t} + u \frac{\partial \eta}{\partial x} + v \frac{\partial \eta}{\partial y} = w, \quad (6)$$

The boundary condition for horizontal velocity  $\vec{V}_h = (u, v)$  is

$$K_M \frac{\partial \vec{V}_h}{\partial z} = \frac{\vec{\tau}}{\rho_0}, \quad (7)$$

where  $\vec{\tau} = (\tau^{(x)}, \tau^{(y)})$  is wind stress. The non-slip boundary conditions were used for the velocity field at the solid boundaries. At the computational layer nearest to the boundary, the logarithmic layer relations were applied. Particularly, for the bottom at level  $z = -H + z_b$ , the boundary conditions are taken in the form:

$$-u \frac{\partial H}{\partial x} - v \frac{\partial H}{\partial y} = w, \quad (8)$$

$$K_M \frac{\partial \vec{V}_h}{\partial z} = \frac{\vec{\tau}_b}{\rho_0}. \quad (9)$$

Here the bottom shear stress  $\vec{\tau}_b$  is specified by

$$\vec{\tau}_b = \rho_0 C_D |\vec{V}| \vec{V}, \quad C_D = \left( \frac{1}{\kappa} \ln \left( \frac{z_b + z_0}{z_0} \right) \right)^{-2},$$

where  $z_0$  is the roughness length,  $\kappa$  is the von Karman constant.

The relevant boundary conditions for equations (4)-(5) also are prescribed at the first computational level at the surface and solid boundaries. They are written for surface and bottom as

$$(q^2(0); q^2(0)l(0)) = (B_1^{2/3} u_*^2(0); 0), \quad (10)$$

$$(q^2(-H); q^2(-H)l(-H)) = (B_1^{2/3} u_*^2(-H); 0),$$

(11)

where  $u_*(0), u_*(-H)$  are friction velocities at surface and bottom, respectively,  $u_*^2(0) = |\vec{\tau}| / \rho_0$  and  $u_*^2(-H) = |\vec{\tau}_b| / \rho_0$ .

At the open boundaries, two types of boundary conditions can be used: radiation conditions (Orlanski 1976) and boundary conditions based on the Newton relaxation technique. The computational domain is a closed area that is divided into an internal zone and relaxation zones along the open boundaries. The boundary conditions at the outer boundary of relaxation zones are non-slip conditions for the velocity field and zero level of turbulence. The modified

equation for surface elevation derived by the integration of continuity equation (1) from bottom to surface is

$$\frac{\partial \eta}{\partial t} + \frac{\partial \bar{u}(H + \eta)}{\partial x} + \frac{\partial \bar{v}(H + \eta)}{\partial y} = -\frac{\eta - \eta_B}{T} \alpha. \quad (12)$$

The depth averaged velocity components are  $(\bar{u}, \bar{v})$ . The right side of equation is the Newton relaxation term, where  $\alpha$  is relaxation parameter, that is  $\alpha = 1$  at the outer boundary of relaxation zone and  $\alpha = 0$  in the internal zone,  $\eta_B$  is the prescribed elevation on the outer boundary and  $T$  is the relaxation time. Large viscosity and diffusivity  $K_r$  was added to the computed values in the relaxation zone. The relaxation time is a parameter chosen to satisfy non-reflecting conditions for disturbances entering into the relaxation zone. The advantage of this approach is that velocities are calculated from the hydrodynamic equations in the closed domain to satisfy the prescribed water level and viscosity in the relaxation zones.

### Discharge induced by vessel propulsion systems

Detailed calculations of flow structures around propellers are a laborious task that is not considered in this paper. Instead a semi-empirical approach based on momentum theory (Blaauw and Van de Kaa 1978) was used to determine discharge generated by the propeller/jet. For slowly maneuvering vessels (the advance speed  $\sim 0$ ) the discharge rate a single propeller  $Q_p$  is

$$Q_p = \sqrt{\frac{\pi K_T}{4\psi}} nD^3, \quad (13)$$

where  $D$  is the propeller diameter,  $n$  is a number of revolutions per second,  $K_T$  is the thrust coefficient of propeller,  $\psi = 2$  for open wheels and  $\psi = 1$  for Kort nozzles. According the momentum theory the free propeller jet is contracted to the diameter  $D_0 = D/\sqrt{2}$  at distance  $\xi_0 = 0.5D$  from propeller whereas with a Kort nozzle the contraction is negligible and  $D_0 \approx D$ . The corresponding velocity  $U_2$  is

$$U_2 = \frac{4Q_p}{\pi D_0^2} = \sqrt{\frac{16K_T}{\pi\psi}} nD \quad (14)$$

Zero flux of turbulent quantities was assumed through the propeller plane

$$\frac{\partial q^2}{\partial \xi} = \frac{\partial l}{\partial \xi} = 0, \quad (15)$$

where  $\xi$  is coordinate in the propeller jet direction.

### Numerical setup

The numerical algorithm was implemented in the horizontal using a curvilinear orthogonal coordinate system. Transformation from the Cartesian coordinates into general vertical coordinates (Mellor et al. 2002) allows flexible and accurate description of the bottom topography. Two vertical system limit cases can be described: quasi- $z$ -system of coordinates and terrain-following sigma-system of coordinates. The quasi  $z$ -system is most appropriate in the case of steep bottom topography with underwater structures whereas the sigma-system is the best for smooth topography.

Finite difference methods were used to solve 2-D equations for surface elevation and depth-averaged velocities (external mode) and 3D equations for velocity, pressure and the transport equations of the turbulence model (internal mode). The effective technique of decomposing the pressure and velocity fields into hydrostatic and non-hydrostatic components was used (Casulli, Stelling, 1998; Kanarska, Maderich, 2003). The surface elevation, hydrostatic and non-hydrostatic components of pressure and velocity are calculated at sequential stages. Unlike most non-hydrostatic models, the 2-D depth-averaged momentum and continuity equations were integrated explicitly, whereas the 3-D equations were solved semi-implicitly at subsequent stages. The finite-difference solutions of governing equations were derived using a four-stage procedure.

In the first stage, the calculation of free surface elevation was performed explicitly from depth-integrated shallow water equations as in the hydrostatic POM model (Blumberg and Mellor 1987). To retain non-hydrostatic dynamics in the free surface field, the initial 2-D velocity fields on each external stage were determined by direct integration of the general non-hydrostatic 3-D velocity fields of the previous internal step.

In the second stage, the 3-D hydrodynamic equations (without the non-hydrostatic pressure component) were solved semi-implicitly with an internal time step to determine provisional values of the velocity field. The advection and horizontal viscosity were discretized explicitly. The three-diagonal system obtained through this process was solved by a direct method.

In the third stage, the non-hydrostatic components of velocity were computed by correcting the provisional velocity field with the gradient of non-hydrostatic pressure to satisfy the continuity equation for the sum of hydrostatic and non-hydrostatic velocities. The discretized Poisson equation obtained this way for the non-hydrostatic pressure was reduced to a non-symmetric 15-diagonal linear system. The preconditioned biconjugate gradient method was used to solve this system. Once the non-hydrostatic pressure was determined, the corresponding components of the velocity fields were calculated.

In the fourth stage, the scalar fields of turbulent energy and length scale were computed using a semi-implicit numerical scheme in the vertical direction. The three-diagonal system obtained this way was solved by a direct method.

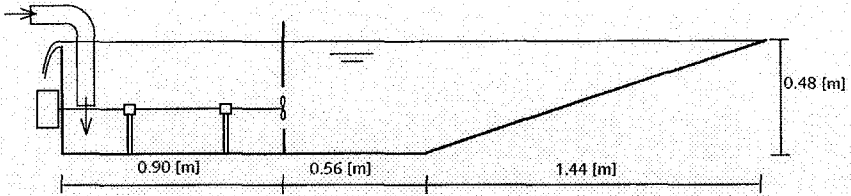


Figure 1. Side view and dimensions of the experimental basin (Schokking 2002).

### SIMULATION OF LABORATORY EXPERIMENT

Simulations of the impacts of a free propeller jet on an inclined bottom in the laboratory tank (Schokking 2002) were carried out. The experimental setup is shown in Figure 1. The tank has dimensions  $2.0 \times 1.9 \times 0.48$  m, with bottom slope 3H:1V. The bottom was covered by gravel with diameter 9.0 mm. A propeller with diameter  $D_0 = 0.1$  m was installed in depth 0.29 m within the barrier that divided the enclosed volume from the accessory volume in which water comes to balance level in both tanks. The excess of water flows away from the tank over both sidewalls.

In the numerical simulations, the jet flowed out through the square hole with size  $8.86 \times 8.86$  cm with an initial velocity of 1.38 m/s, which corresponds to the jet velocity and discharge in the experiment. At the lateral walls of the basin, the Newton relaxation boundary conditions were used. The grid resolution in the model was  $101 \times 101 \times 39$  using a sigma vertical coordinate system. Figure 2 shows computed vertical velocity profiles along the jet axis compared with measurements in the steady-state flow. The model results agree with the experiments. The complicated structure of the velocity field is shown in Figure 3 where longitudinal and transverse velocity fields are presented in two cross-sections. At the cross-section nearest to the propeller ( $x = 0.5$  m) over the horizontal bottom, the jet is already affected by bottom and has an elongated cross-section. At greater distance from the propeller ( $x = 0.95$  m), the jet is spread over the slope with a strong transverse circulation caused by the bottom topography.

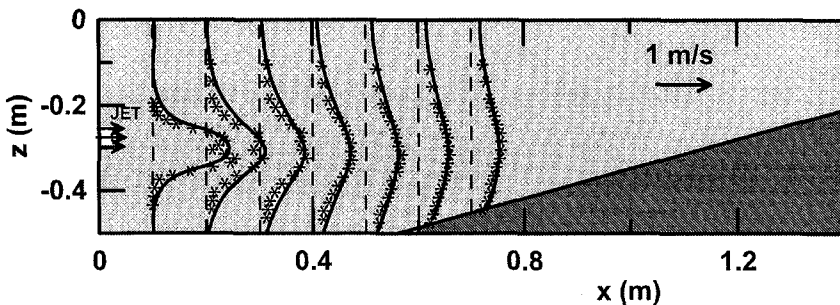


Figure 2. Computed vs. measured (Schokking, 2002) vertical distribution of mean velocities along the jet axis.

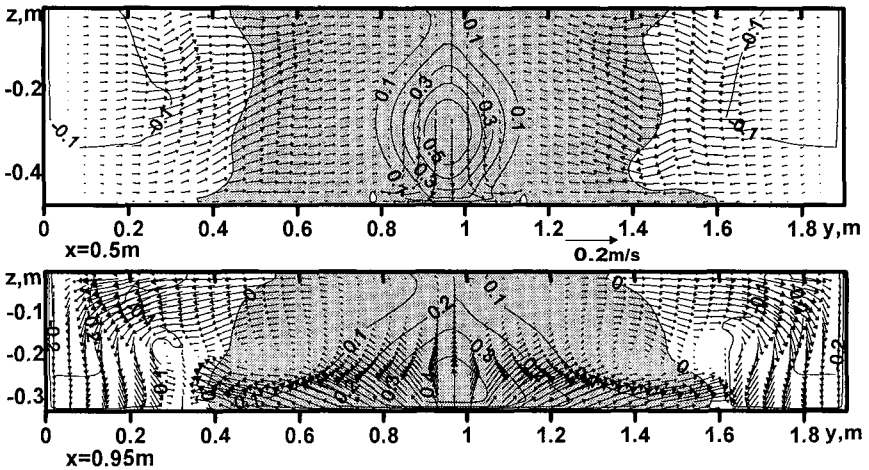


Figure 3. Cross-sections of simulated velocity at  $x=0.5\text{m}$  (a) and  $x=0.95\text{m}$ . The isolines of longitudinal velocity component  $u$  and the arrows represent transverse velocities.

Figure 4 shows the calculated normalized bottom shear stress

$$\bar{\theta} = \frac{\bar{\tau}_b}{g(\rho_s - \rho_0)d} \quad (16)$$

for steady-state flow. Here  $\rho_s$  is sediment grain density. The value  $|\bar{\theta}| = \theta$  is the non-dimensional Shields parameter (Shields 1936) that represents the ratio of shear stress force applied to the layer of grains to the stabilizing gravity force. As shown in figure the maximum of  $\bar{\theta}$  is located around the point of intersection of the jet axis and the inclined bottom and along the side of the tank opposite the propeller. The majority of sediment transport models assume that sediment motion occurs when  $\theta$  exceed some critical value  $\theta_{cr}$ . In the experiment of Schokking (2002), tests were performed to investigate damage to the bottom covered by gravel with diameter 9 mm due to the propeller jet. The results of the experiment show that the maximum damage on the slope occurs on the lower part of the slope, approximately between 0 and 0.10 m above the toe (rectangle in Figure 4), and therefore shear stress force alone cannot be responsible for damage. Moreover the gravel motion in the lower part of the slope occurred in the normal or even opposite to the jet flow direction (Figure 5a). Schokking (2002) presumed that this damage is caused by the gradients in pressure forces.

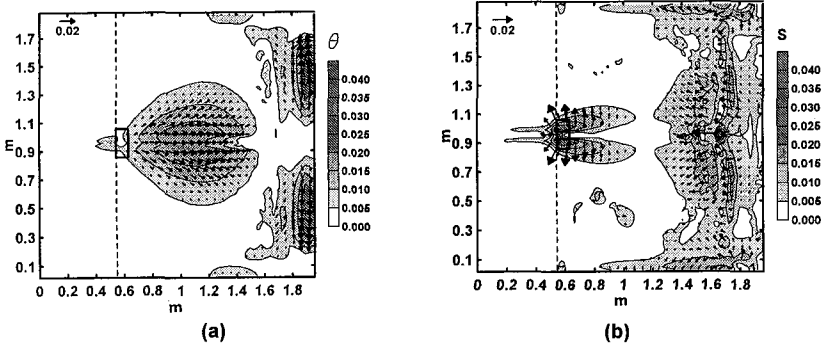


Figure 4. Calculated normalized bottom shear stress  $\bar{\theta}$  (a) and dynamic pressure gradient  $\bar{S}$  for free propeller experiment. The dashed line shows toe of inclined bottom and rectangle shows zone of maximal damage (Schokking 2002).

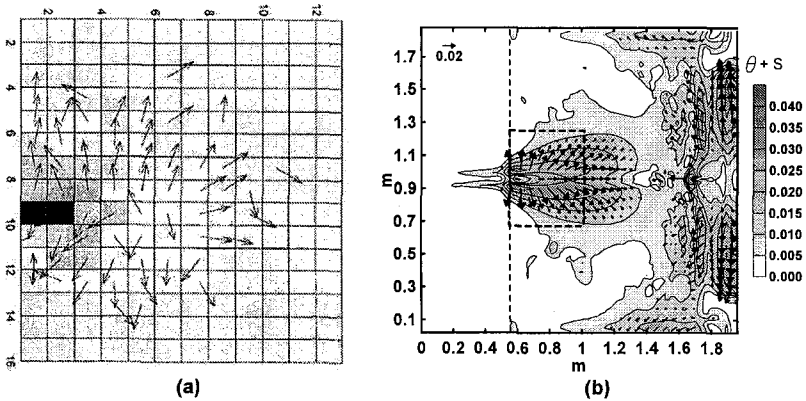


Figure 5. Movement of stones in experiment of Schokking (2002) (a). Calculated sum of normalized bottom shear stress and dynamic pressure gradient (b). The dashed rectangle corresponds to the area in (a).

The model allows us to quantify this hypothesis by calculating the normalized gradient of dynamic pressure  $\bar{S}$  as:

$$\bar{S} = -\frac{\nabla p}{g(\rho_s - \rho_0)}, \quad (17)$$

The value  $S = |\bar{S}|$  is the non-dimensional Sleath parameter that was introduced by Sleath (1999) to characterize incipient motion of sediment under waves. Figure 4b shows that the experimentally determined zone of damage coincides with the computed zone of maximum values of  $S$ . The direction of gravel movement in the experiment (Figure 5a) agrees with the direction of the pressure gradient force shown in Figure 4b.

Figure 5b shows vectorial sum of both forces acting on sediment, which is described by:

$$\bar{\theta} + \bar{S} = \frac{\bar{\tau} - d\nabla p}{g(\rho_s - \rho_0)} \quad (18)$$

It should be emphasized that the maximum propeller/jet current forces acting on inclined bottom slopes occurs on two sides on jet axis. Another zone of propeller wash is related with shallow near coast area. We conclude that in the future, sediment transport models should be modified by inclusion of a mechanism of pressure gradient-induced transport to properly describe erosion caused by propeller jets.

## SIMULATION OF FIELD EXPERIMENTS

The VH-PU model was also preliminarily validated using a set of measured field current data from tug boat propwash. Figure 6 shows the test setup with Acoustic Doppler Current Profiler mounted on the bottom in approximately 10m water depth. The vessel position was tightly controlled with Differential GPS and precise correlation between gage and boat times were maintained.

The simulations were carried out in a modeling domain 20x30 m with resolution in the sigma system of 101x91x40. Testing showed that precise control of the tug boat direction as it began moving away from the measurement site was critical, since at relatively short distances from the gauge (10m), small errors in vessel heading changed the location of the velocity jet, preventing the largest velocities from being measured by the ADCP. For testing runs where the tug position was well-controlled and the jet was directed over the ADCP, the simulations agree with the vertical distribution of mean velocities along the jet axis (Figure 7). The velocities shown in Figure 7 were generated by a tug vessel

with propeller diameter 1.83m, thrust 74,000 N, initial velocity 5.25 m/s with the propeller rotating at 200 RPM.

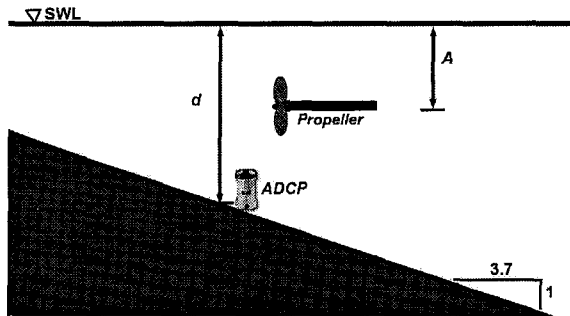


Figure 6. Setup of field test.

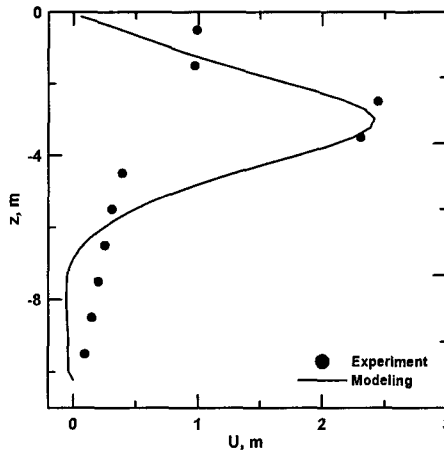


Figure 7. Vertical distribution of velocities along the jet axis at time=5 sec. The curve is VH-PU model computations, symbols are field measurements (2-second averages).

### EXAMPLE APPLICATION

The VH-PU model has been successfully used on a number of projects in CA, WA, TX and LA. Ferry terminals in Puget Sound are often located adjacent to aquatic habitat or other marine resources, therefore upgrades and/or new construction of these terminals requires thorough analysis of propwash impacts to marine resources. Washington State Ferries (WSF) is planning to upgrade the terminal at Port Townsend, Puget Sound, WA. It was determined that eelgrass was present on the sea floor around the ferry terminal; therefore analysis of potential propeller wash impacts was initiated.

Figure 8 shows bottom velocities predicted by the VH-PU model for an Issaquah-class ferry landing at the terminal, as well as the locations of eelgrass and depth contours. The model's predicted bottom velocities were reasonable and the locations of high velocities corresponded to the locations where eelgrass was not present, i.e. velocities are above threshold for eelgrass survival. Model results were used to determine distinct areas of potential scour for various sediment sizes and areas of likely propeller wash damage to eelgrass.

Other VH-PU model applications include evaluation of propeller-induced velocity on slopes at marine terminals for sizing rock slope protection, as well as evaluating bottom velocities due to propeller wash and required sediment sizes for capping of contaminated sediments.

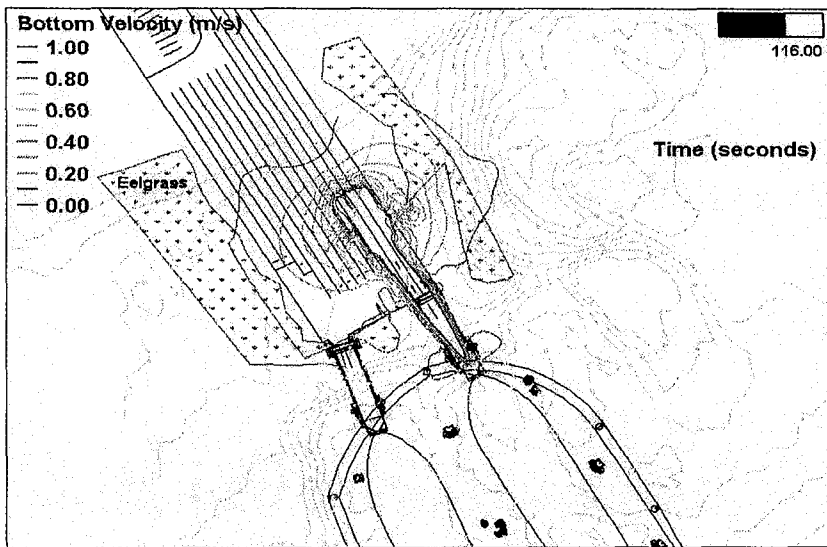


**Figure 8. Bottom velocities generated by Issaquah-class ferry during landing at Port Townsend ferry terminal, Puget Sound, WA at simulation time = 116 sec. Also shown are bottom elevation contours, eelgrass locations and terminal and vessel locations.**

## CONCLUSIONS

A new three-dimensional non-hydrostatic free-surface numerical model VH-PU based on the Reynolds averaged Navier-Stokes equations model was presented to predict action of the propeller jet of slowly maneuvering ship on the bottom and bank. The results of simulations show good agreement with the laboratory experiments in the tank with inclined bottom (Schokking 2002) and field measurements. The simulations confirm that damage to slope protection can be caused by combined action of the pressure gradient and shear stress.

## ACKNOWLEDGMENTS

The VH-PU model development was partially sponsored by the U.S. Civilian Research and Development Foundation (Project UKG2-582-KV-05).

## REFERENCES

- Blaauw, H.G., van de Kaa. 1978. Erosion of bottom and sloping banks caused by the screw-race of manoeuvring ships. *International Harbour Congress*, Antwerp, Belgium, 1-16.
- Blumberg, A.F. and G.L. Mellor. 1987. A description of a three-dimensional coastal ocean circulation. *Three-Dimensional Coastal Ocean Models*, N. Heaps (ed), Washington, D.C., Am. Geoph. Union, 1-16.
- Casulli, V. and G.S. Stelling. 1998. Numerical simulation of 3D quasi-hydrostatic, free-surface flows. *J. Hydr. Eng.* 124, 678–686.
- Fuehrer, M., Pohl, H. and K. Roemisch. 1987. Propeller jet erosion and stability criteria for bottom protections of various constructions. *Bulletin of the PIANC*. No. 58, 45-56.
- Hamill, G.A. 1988. The scouring action of the propeller jet produced by a slowly manoeuvring ship. *Bulletin of the PIANC*, No. 62, 85-110.
- Kanarska, Y. and V. Maderich. 2003. A non-hydrostatic numerical model for calculating free-surface stratified flows. *Ocean Dynamics*, 53, 176-185.
- Mellor, G. L., S. Hakkinen, T. Ezer and R. Patchen. 2002. A generalization of a sigma coordinate ocean model and an intercomparison of model vertical grids, In: *Ocean Forecasting: Conceptual Basis and Applications*, N. Pinardi and J. D. Woods (Eds.), Springer, Berlin, 55-72.
- Mellor, G. and Yamada, T. 1982. Development of a turbulence closure model for geophysical fluid problems. *Reviews of Geophysics and Space Physics*, 20, 851-875.
- Orlanski, V.P. 1976. A simple boundary condition for bounded hyperbolic flows. *J. Comp. Phys.* 54, 325–362.
- Schokking, L. 2002 *Bowthruster-induced Damage*. MS thesis. Technical University Delft, Delft, 143pp.
- Shepsis, V. and D. Simpson. (1999). Propwash modeling for CAD design. Conference on Dredged Material Management: Options and Environmental Considerations, Boston, MS, December 6-9, 2000
- Shields, A. 1936. Anwendung der anlichkeitsmechanik und turbulenzforschung auf die geschiebebewegung. *Mitt. Preuss. Versuchsanstalt fur Wasserbau und Schiffbau.*, 26.
- Sleath J.F.A. 1999. Conditions for plug formation in oscillatory flow. *Cont. Shelf Res.*, 10, 1643-1664.
- Verhey, H.J. 1983. The stability of bottom and banks subjected to the velocities in the propeller jet behind ships. *Proceedings of the 8th International Harbour Congress*. Publication No 303, Antwerp, Belgium, 1-11.
- Vollmers, H. and J.C. Rotta. 1977. Similar solutions of the mean velocity, turbulent energy and length scale equation. *AIAA J.*, 15, 714-720.